Journal of Magnetism and Magnetic Materials 505 (2020) 166762

Contents lists available at ScienceDirect

Journal of Magnetism and Magnetic Materials

journal homepage: www.elsevier.com/locate/jmmm

Research articles

Analytical calculation of magnetic field components in synchronous reluctance machine accounting for rotor flux barriers using combined conformal mapping and magnetic equivalent circuit methods

Moein Farhadian[a,*], Mehdi Moallem[a], Babak Fahimi[b]

[a] Department of Electrical and Computer Engineering, Isfahan University of Technology, Isfahan, Iran
[b] Department of Electrical and Computer Engineering, University of Texas at Dallas, Richardson, USA

ARTICLE INFO

Keywords:
Synchronous reluctance motor
Analytic model
Conformal mapping
Magnetic equivalent circuit

ABSTRACT

Despite many efforts being devoted to simplify the analysis of Synchronous Reluctance Motors (SynRM), the use of analytical methods to calculate torque ripple in these machines remains an ongoing challenge. In this paper, the electromagnetic characteristics of a SynRM are obtained using the combined conformal mapping (CM) and magnetic equivalent circuit (MEC) method. The proposed combination makes it possible to take into account the effects of stator slots and rotor flux barriers (FBs) in modeling of the radial and tangential field components. This is accomplished by introducing virtual currents in the CM model to account for rotor potential drops due to the presence of FBs. These potential drops are calculated using the MEC model. Once specified, the field components are used to calculate the SynRM torque with three FBs. Finally, the accuracy of the proposed method is validated by comparison with finite element analysis results.

1. Introduction

Simple rotor structure, reduced rotor losses, ease of control, and enhanced power density are among the prominent properties of Synchronous Reluctance Motors (SynRM). These attributes have attracted substantial attention in recent years to SynRM as a potential contender to replace induction motors [1].

The main challenges facing the design of these machines include the determination of rotor geometry and the arrangement of flux barriers (FBs) so as to achieve proper motor torque characteristics. In this regard, the location of FBs influences the shape of the air gap field by a significant margin. Moreover, rotor structure, if not properly designed, can generate large torque ripple, thereby disrupting proper operation of the motor.

The Finite Element Method (FEM) is a common technique used for analyzing electric machines. In [2], FEM was combined with a multi-objective evolutionary optimization technique to improve the SynRM torque characteristics. The systematic sensitivity analysis approach to SynRM design based on a limited number of FE analyses is presented in [3]. In this method, the final solution is not necessarily an optimal one; rather, the analytical method is combined with FEM to reduce the computation time as a direct result of reducing the number of machines to be evaluated. Despite its highly accurate results, FEM suffers from such disadvantages as high computational time and the requirement for constructing a geometrical model for each iteration within an optimization algorithm. Analytical methods are, therefore, highly desirable as they allow a large number of analyses to be performed within a relatively much shorter period of time.

Commonly used for calculating the inductances of the d and q axes and the average torque value of a SynRM, the Magnetic Equivalent Circuit (MEC) can be effectively employed for the quick evaluation of machine performance [4,5]. However, the method, when used alone, cannot estimate the distribution of the magnetic field in the air gap or torque ripple accurately unless a highly compressible grid network is considered, in which case it will not be dramatically different from the FEM in terms of computational complexity. These considerations have motivated combinations of the MEC and other computational methods [6,7].

An analytical method was presented in [6] for the SynRM motor in which the MEC model was used only for the rotor. In this method, the magnetic potential in the SynRM rotor is obtained by the MEC method based on the function of the stator magnetic potential expressed in terms of the Fourier series expansion. Using the differential of the rotor and stator potentials, the radial component of the magnetic field is obtained in a uniform (i.e., smooth with no slots) air gap and was further used to calculate torque. A similar analytical method using the

* Corresponding author.
E-mail address: moein.farhadian@ec.iut.ac.ir (M. Farhadian).

https://doi.org/10.1016/j.jmmm.2020.166762
Received 22 November 2019; Received in revised form 7 March 2020; Accepted 17 March 2020
Available online 19 March 2020
0304-8853/

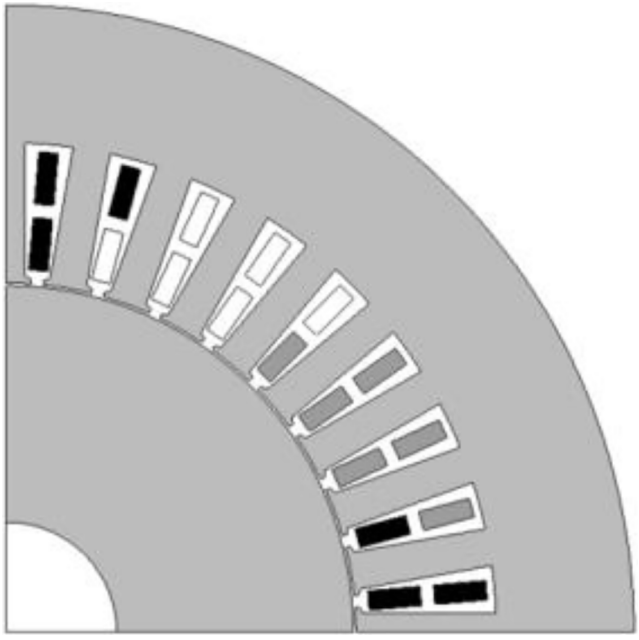

Fig. 1. One pole of study motor without flux barrier.

Table 1
Geometric parameters of the SynRM.

Rotor inner radius	20 mm
Rotor outer radius	63 mm
Stator slot bottom radius	89 mm
Stator outer radius	114 mm
Air gap thickness	0.5 mm
Number of pole pairs	2
Number of stator slots	36
Number of conductors per slot	60
Number of winding layers per slot	2
Slot opening width	2°
Core length	200

winding function in the stator model and the MEC for the rotor model was proposed in [8] to calculate the radial air gap field of the SynRM which took into account the effect of stator slots via the non-dimensional permeance function. Studies have also been devoted to including saturation effect in the SynRM's analytical modelling [9,10]. However, the proposed methods are not capable of accurately calculating torque ripple as they fail to account for the tangential component of the magnetic field in the air gap.

The Conformal Mapping (CM) technique is capable of accurately estimating both radial and tangential magnetic field components of the machine. This method has been recently used for the analysis of a variety of machines including Induction motors [11], surface and inset mounted permanent magnet motors [12,13], and Switched Reluctance motors [14]. Efforts have also been made to combine both CM and MEC techniques [15]. In [16], for instance, the air gap field for the interior permanent magnet motor is obtained by MEC based on a uniform air gap. This is followed by employing the CM method to account for the effect of flux concentration on the stator teeth in order to include the effect of stator slots in the computation of the magnetic field. In other studies [17,18] these two methods were combined and two separate magnetic circuits were considered for the rotor and stator of the surface permanent magnet motor. In this way, the effect of iron saturation is accounted for in the calculation of both the cogging torque and the back EMF.

The CM method and its ability to complement other methods has made it a useful tool for analysis of SynRM machines by calculating the circular [19] and Zhukovski shaped [20] FB reluctance and for determining the effect of stator [21] and rotor slots [22] in the radial component of air gap field via the permeance functions. In previous works [6,8,19–22], field changes were only considered along a radial component.

In this paper, the tangential and radial components of the SynRM air gap field are obtained using a combination of the CM and MEC methods. Using the Schwarz-Christoffel (SC) mapping and the analytical solution of the field, flux density is initially obtained for the air gap while the FBs are ignored. The MEC method is then employed to calculate the potential drop due to FBs using the field obtained from the CM method in the previous step. The effect of FBs on the tangential component of the field is also obtained by considering the potential drop of the FBs which is modeled as virtual currents in the CM method. Once specified, the field components are used to calculate motor torque. Finally, the accuracy of the proposed method is evaluated via FE analysis. The only simplifying assumption in the model lies with neglecting saturation effect in rotor and stator core.

The rest of the paper is organized as follows: Section 2.1 provides a brief description of the CMs used and the computed field for a motor without FBs. Section 2.2 describes the calculation of MEC elements and rotor potential drop. Section 2.3 shows how the FB effect is added to the field. This section further describes the assumptions used in the proposed method. Section 3 employs the proposed method to calculate the SynRM torque with three flux barriers and compares the results with those obtained from FEM.

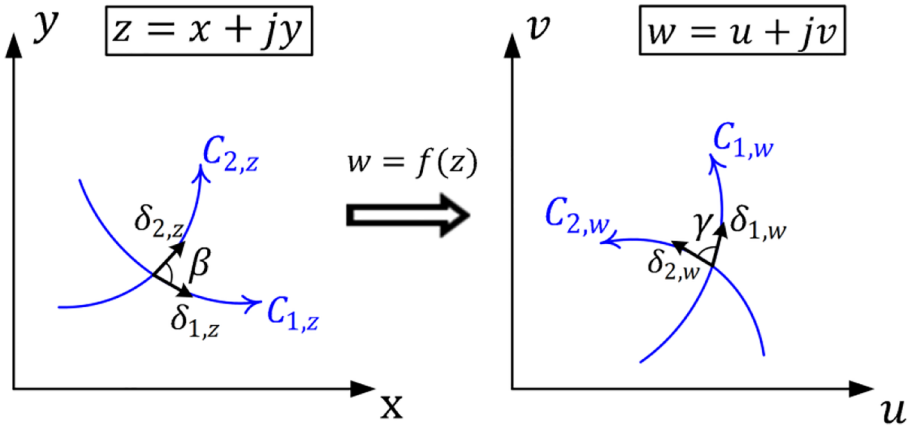

Fig. 2. Curves $C_{1,z}$ and $C_{2,z}$ and their respective images $C_{1,w}$ and $C_{2,w}$ under a CM w = f(z).

2. Material and methods

2.1. Conformal mapping and analytical calculation of stator field

In this Section, the stator field of a four-pole SynRM shown in Fig. 1 is obtained using the CM method while the rotor FB is ignored. The main geometrical properties of the SynRM are given in Table 1. The advantage of the CM is that an analytical field solution of the boundary value problem can be obtained for a complex motor geometry. This is accomplished by mapping the original geometry of the motor onto a simple one that yields the boundary value problem solution. Once the solution is obtained, it is mapped back to the original geometry.

A mapping between two planes Z and W is called conformal if it preserves angles between oriented curves in magnitude as well as in direction. In Fig. 2 which shows the CM of the two planes the angles β and γ are identical.

CM keeps the distribution of magnetic potentials in different complex planes unchanged. The potential lines and the field around the current conductor remain perpendicular. Also, boundary conditions do not change under the transformation of variables dependent on the CM. In this paper two CMs shown in Fig. 3 are employed to reach the canonical (rectangular) domain. The main CM is the SC, which is used to transform the complex geometry of the motor into an area where the solution of the field is achievable. Using this CM, one can convert the inner region of a polygon into a disk, rectangle, upper half of the plane, or bi-infinite strip. Because the motor geometry is curved in the initial coordinates, it is necessary to first convert the curved geometry of the motor into straight lines of a polygon. This is done by logarithmic CM.

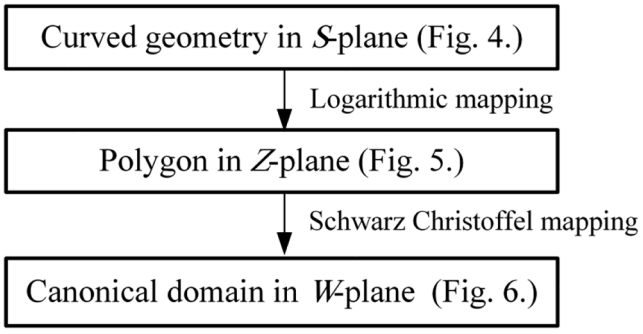

Fig. 3. Steps of CMs.

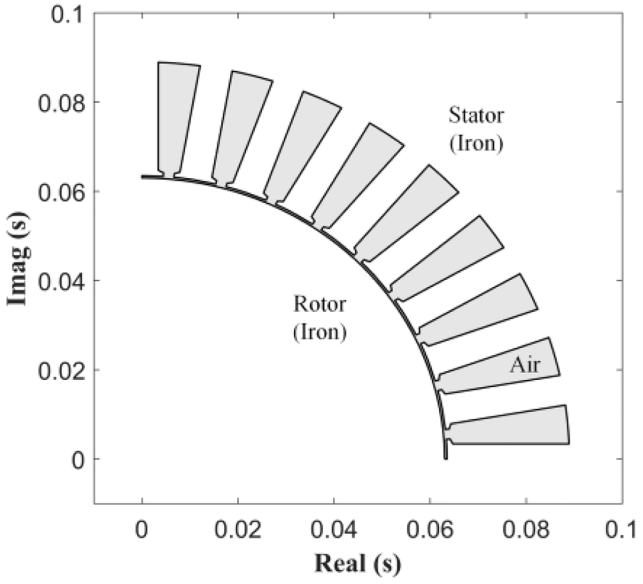

Fig. 4. Study model in S-plane.

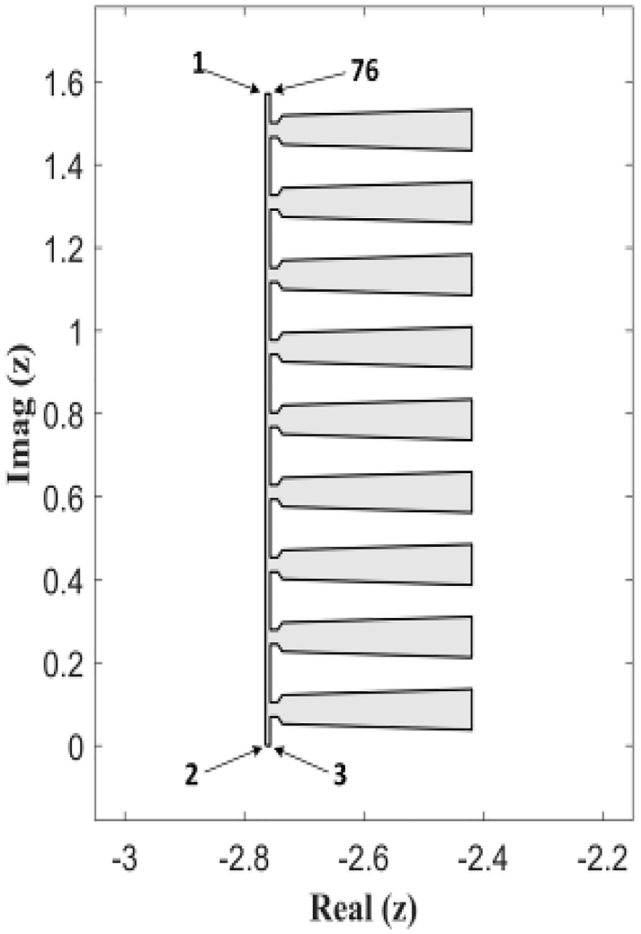

Fig. 5. Study model in Z-plane.

2.1.1. Logarithmic conformal mapping

The first CM to be used is the complex logarithmic function expressed by (1) given below:

$$z = \log(s) \tag{1}$$

By applying this CM, the curve-shaped geometry of the motor in the S-plane (Fig. 4) is mapped into a polygon in the Z-plane with 76 vertices (Fig. 5).

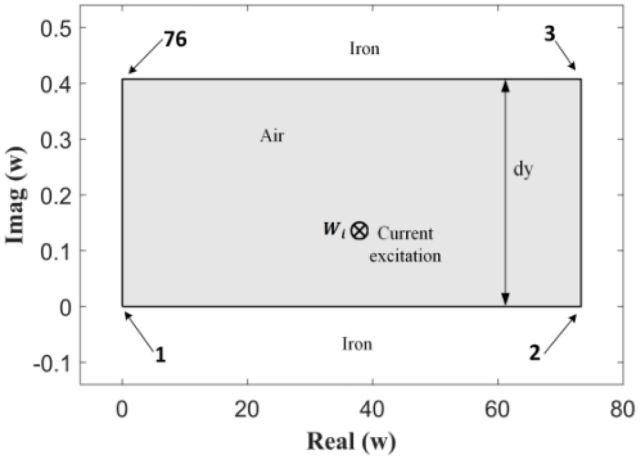

Fig. 6. Study model in W-plane (Rectangular domain).

2.1.2. Schwartz Christoffel mapping

The SC mapping defined by (2) is used to map the interior region of the polygon into the upper half of the plane and boundary of the polygon onto the real axis [23].

$$z = f(w) = A\int \prod_{k=1}^{n-1} (w - w_k)^{-\frac{\alpha_k}{\pi}} dw + C \tag{2}$$

where A and C are arbitrary integration constants and n is the number of polygon corners. $w_1, \cdots, w_n$ are the points in the canonical domain (in the W-plane) corresponding to the polygon corners and α_k represents the interior angles of the polygon. The SC integral can be modified to map the air region (grey area in Fig. 5) of the motor polygon into the rectangle shown in Fig. 6 for the canonical domain. For simple geometries having three vertices, the integral solution can be found analytically, but for polygons with more than three vertices, the integral solution must be obtained by numerical methods. The calculations for the numerical solution of the SC integral are accomplished using the SC MATLAB toolbox. The command line functions in this toolbox allow the user to obtain a polygon mapped to the desired canonical domain (a rectangular domain in our case) by selecting the source polygon and the relevant functions. More information on the SC Toolbox may be found in [24].

2.1.3. Analytical solution of the stator field

The inner quadrant polygon motor is mapped onto a rectangle in the W-plane from the mappings described above. In this simple domain, the current conductors lie between the two infinite iron plates. The field generated by each current conductor is obtained using (3) [13]:

$$B_w = j\frac{I_i \mu_0}{4dy}\left[\coth\left(\frac{\pi}{2dy}(w - w_i)^*\right) + \coth\left(\frac{\pi}{2dy}(w - w_i^{*})^*\right)\right] \tag{3}$$

where w_i represents the coordinate points on which the conductors with

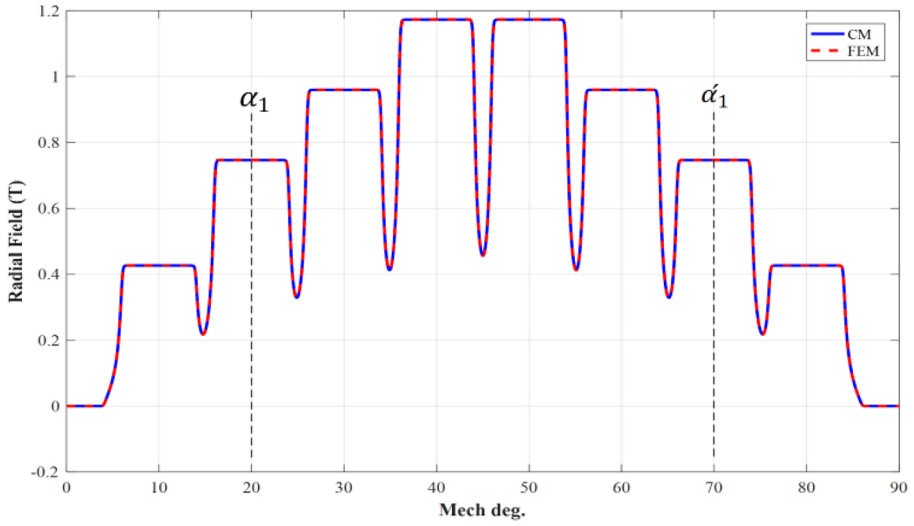

Fig. 7. Radial field component of smooth rotor in the middle of air gap.

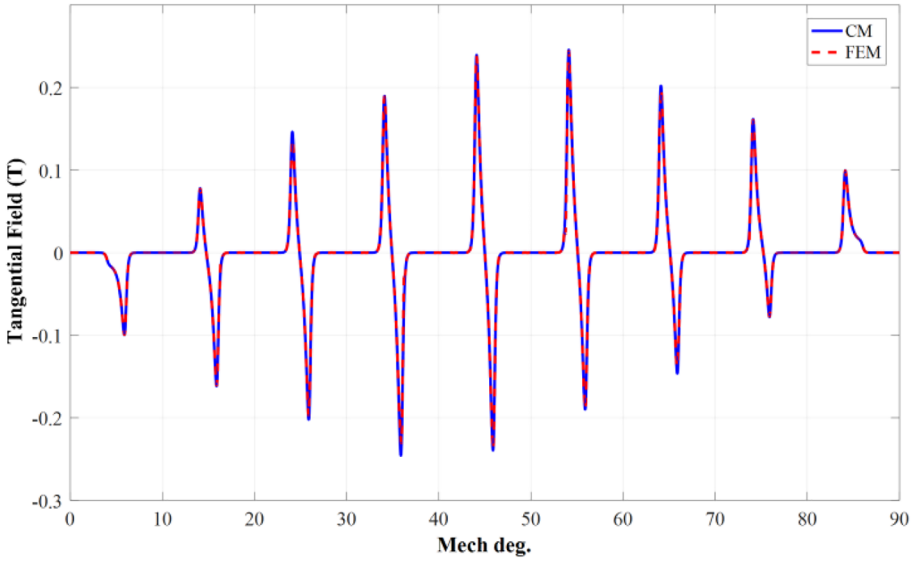

Fig. 8. Tangential field component of smooth rotor in the middle of air gap.

the current I_i are located and w represents the coordinates of the points in air gap for which the field is to be calculated. The asterisk (*) represents a complex conjugate operation. The relationship between the field on the W and Z coordinate planes is expressed by (4) [13]:

$$B_z = B_w\left(\frac{\partial w}{\partial z}\right)^* \tag{4}$$

where $(\partial w/\partial z)$ provides the derivative of w with respect to z. Finally, the radial and tangential components of the field are obtained as shown in (5) given below:

$$B_r = \text{real}(B_z)\ and\ B_t = \text{Imag}(B_z) \tag{5}$$

Assuming that the motor windings are driven by a current of 4 amps in the q-axis direction and that the rotor FBs are ignored, the radial and tangential field components in the middle of the air gap for one pole of a SynRM with the specifications given in Table 1 will be the same as those shown in Figs. 7 and 8, respectively. Notably continuous lines represent the field calculated by the CM method and the dashed lines represents the field computed using FEA.

Clearly, there is a good agreement between the results obtained from CM and FEA methods where an infinitely large permeability is assumed. The stator slots cause a dip in the field for the radial components while they cause a change in the field direction in the tangential components. Comparison of the CM and FEA results reveals that the CM method is capable of accurately predicting the effect of stator slots in the air gap field. In what follows, the radial component of the field is used to calculate the sources of flux in the MEC model. It should be noted that unlike Fourier series based approaches for the field calculation [6,8,20–22] that have oscillations in field waveform due to neglecting high order harmonics, the solution of field obtained with conformal mapping is in closed form and smooth.

2.2. MEC model and calculation of flux barrier potential drop

The purpose of this section is to introduce a simple MEC model for the rotor in order to obtain the crossing flux, reluctance, and potential drop due to any FBs. The ampere turns equal to this potential drop are applied subsequently to include the effect of FB on the air gap field. The MEC model is the same as the one given in [6,8] for the SynRM. For the sake of simplicity, the MEC model thus obtained for a rotor with one FB, shown in Fig. 9, can be extended to one with a greater number of FBs. The MEC model for this rotor is the one shown in Fig. 10.

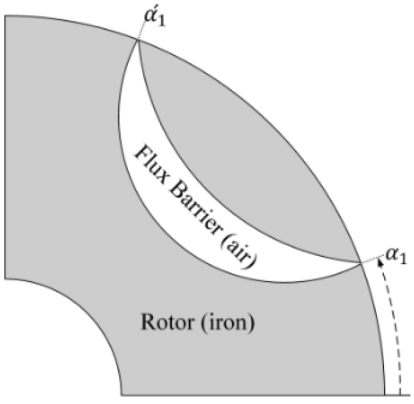

Fig. 9. SynRM rotor with a flux barrier.

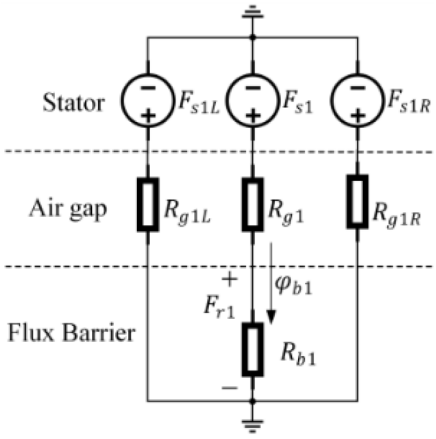

Fig. 10. MEC model of SynRM with one barrier per pole.

2.2.1. Reluctance elements MEC model

In the MEC shown in Fig. 10, iron permeability is assumed to be infinite and only the reluctance of the linear parts of the motor is considered. R_{b1} is the magnetic resistance of FB with respect to its circular shape. Its reluctance is calculated using the *Arc* tan CM [8]. R_{g1}, R_{g2L}, and R_{g2R} represent the air gap resistances. R_{g1} is the reluctance of the air gap $(\alpha_1' - \alpha_1)$which includes FB. R_{g2L} and R_{g2R} have equal values and the rest of the air gap lengths $(\pi/p - (\alpha_1' - \alpha_1))$ are included.

2.2.2. MMF sources in the MEC model

In order to calculate the MMF sources, the MEC model uses the radial field component obtained in the previous section with regard to the effect of the slots ($B_{r\_slotted\_CM}$). The tooth ends have a lower reluctance than the lower portion of the open slots, causing the flux to concentrate on the teeth surface. The effect of flux concentration in [16] was calculated by introducing a flux concentration coefficient (K_{con}) based on the ratio of flux at the teeth level for the model with slots to that for the model without slots. The radial field component is, therefore, modified to compute MMF sources as in (6) [16]:

$$B_{r\_slotted} = B_{r\_slotted\_CM} \cdot K_{con} \tag{6}$$

The ampere turn of the applied arc on the rotor $F_{s1}(t, \theta_r)$ is obtained by integration of the stator field as given in (7).

$$F_{s1}(t, \theta_r) = \frac{g}{\mu_0} \cdot \frac{1}{(\alpha_1' - \alpha_1)} \int_{\alpha_1}^{\alpha'_1} B_{r\_slotted}(t, \theta_r) d\theta \tag{7}$$

Using the parameters of the MEC model, the crossing flux of the FB (φ_{b1}) is obtained. The calculated drop in the potential of the rotor $F_{r1}(t, \theta_r)$ is equal to the flux passing through the FB multiplied by its reluctance value (8) as a function of the stator air gap field.

$$F_{r1}(t, \theta_r) = R_{b1} \cdot \varphi_{b1} \tag{8}$$

2.3. Effect of the flux barrier on the air gap field

The presence of a rotor FB brings about changes in the air gap field, which are different at the end points and along the step of the FB bar. Therefore, they need to be investigated separately.

2.3.1. Field drop

The air gap field in the FB area drops along the air gap. By

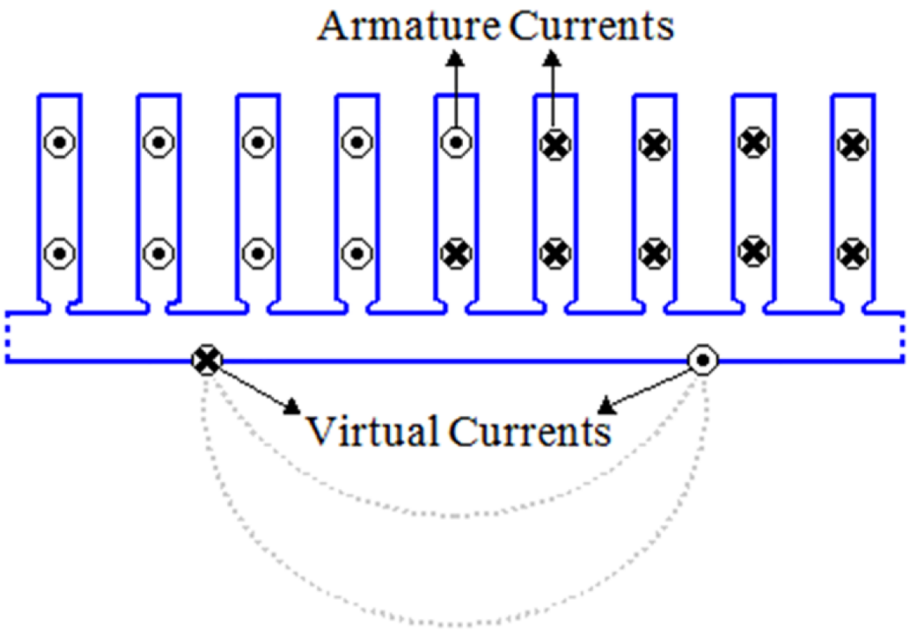

Fig. 11. Position of virtual currents for modelling flux barrier.

distributing the potential FB drop along the radial component of air gap field, the field drop (ΔB) will be obtained only in the radial direction. The presence of FB, however, brings about changes in the tangential field component as well. Subsequently, the potential drop of FB with I_{FB1} virtual currents observed at both ends of each FB (Fig. 11) will be equal to the drop in the magnetic potentials of the rotor (9). Finally, the effects of FB on both the radial and the tangential field components are also determined.

$$I_{FB1} = F_{r1} = R_{b1} \bullet \varphi_{b1} \tag{9}$$

The virtual currents mimic the effects of FBs and create a field, $B_{fluxbarrier}$, which is opposite to the direction of the stator air gap field. The total air gap field, B_{airgap}, will be the sum of the field created by the stator winding, B_{stator}, and the virtual currents representing the FB (10).

$$B_{airgap} = B_{stator} + B_{fluxbarrier} \tag{10}$$

In this Relation, B_{stator} and $B_{fluxbarrier}$ are complex quantities. So the real value of B_{airgap} is equal to the radial component while its imaginary part is equal to the tangential component of the field. Figs. 12 and 13 show the radial and tangential components of the field (B_{airgap}), in which the effect of FB is also taken into account.

As shown in Fig. 12, the radial field drops by one step from the air gap where the FB (from 20 to 70 degrees) is located. This field drop has a constant value in the radial direction.

Comparison of the results obtained via the proposed method and the fields calculated through the FEA for the rotor in Fig. 9 reveals that the proposed method yields a proper approximation of the field potential drop.

The effect of field drop on the tangential component is also evident in Fig. 13. It is worth noting that the sharp change in the tangential field component at the end of the FB in the air gap is well approximated when the drop in the potential of FB is modeled via virtual currents.

For a better illustration of the concept of virtual currents used in modeling the effect of FB, the flux lines for the actual FB are drawn in Fig. 14a and the point (virtual) currents for FB in Fig. 14b. The shape of the flux lines at the ends of the FB in the air gap in Fig. 14a indicates that the reason for the creation of tangible tangential components at these points is the fact that a portion of the rotor flux at the end of the

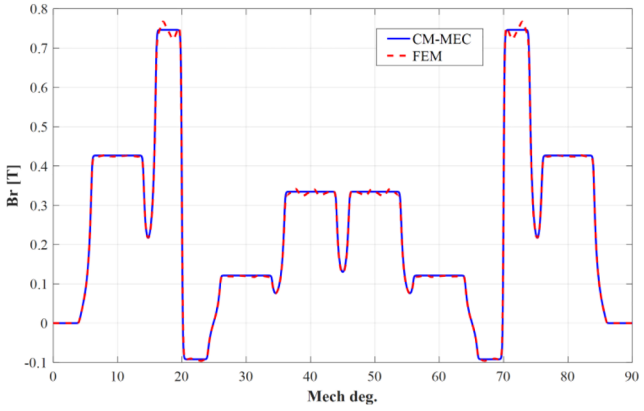

Fig. 12. Radial field component considering flux barrier.

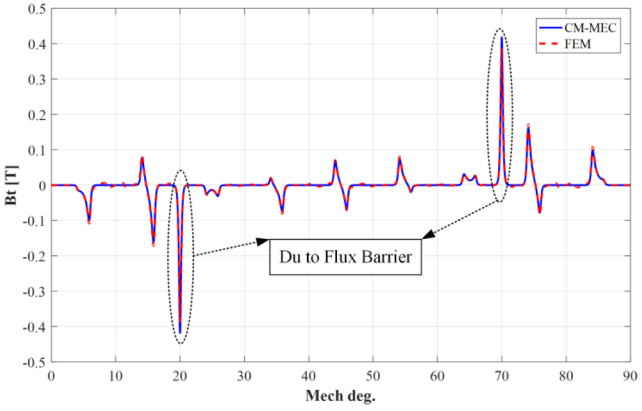

Fig. 13. Tangential field component considering flux barrier.

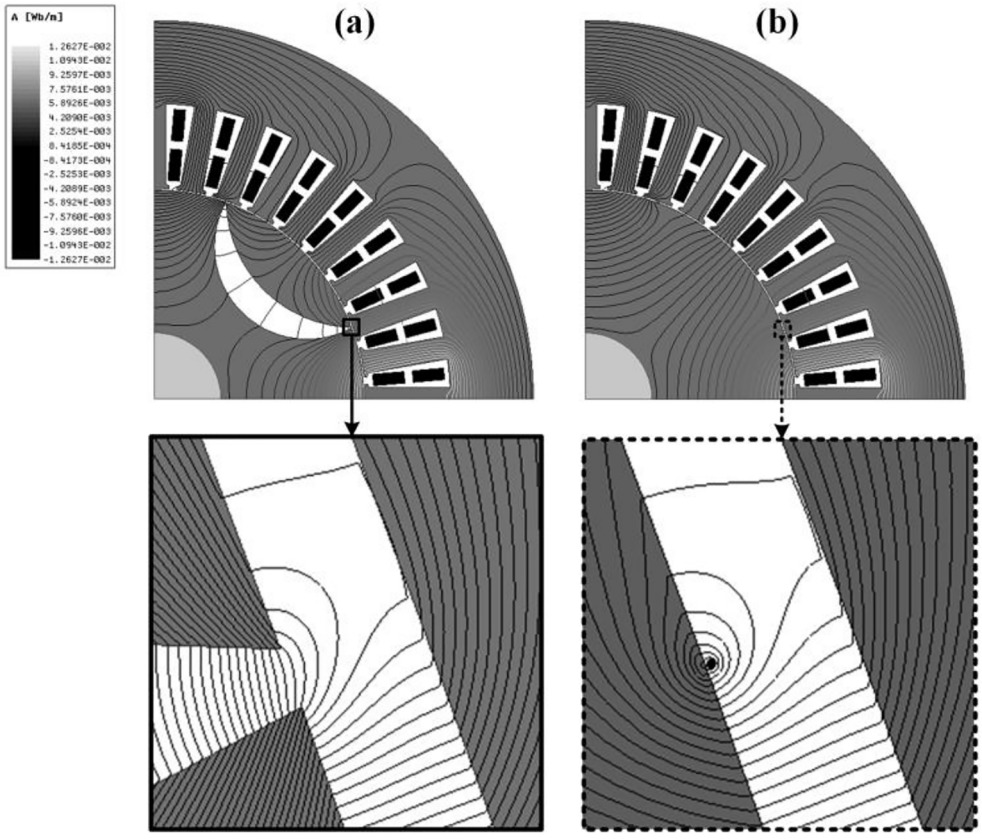

Fig. 14. Flux lines at the end of flux barrier in air gap in actual FB model (a) and virtual FB model (b).

FB does not flow directly into the stator. Instead it turns around the FB and selects its direction again relative to the rotor. As shown in Fig. 14b, the lines of the flux generated by the virtual current are very similar to the actual FB effect and can imitate its effect. In other words, the effects of radial field drop and the severe variations in the tangential field at the end points of the FB can be duly considered if the effect of the potential drop due to FB (calculated by MEC method) is represented by the virtual current ampere turn.

2.3.2. Air gap permeance change

Although ribs are located at the ends of the FB to ensure the mechanical strength of the rotor, iron is saturated in these ribs and, in fact, it can be replaced with air in the model. These end points have the same effect as the slot openings in that they create notches in the air gap field waveform. Using the SC mapping, one can determine the effect of rotor slots in the same way as used for the stator slot using the permeance functions [16]. Thus, the normalized values of FB permeances are multiplied by the air gap field to obtain the permeance effects of FBs on the air gap field (11).

$$B_{ag\_new} = B_{airgap} \quad \lambda(r, \theta)^* \tag{11}$$

where $\lambda(r, \theta)$ is the normalized permeance of the rotor slot, and B_{ag_new} is the air gap field, with the permeance effect of the rotor slot included.

Fig. 15 shows the geometry of a half FB on the *Z*-plane. Because of the circular shape of FB, it is approximated as a polygon with a number of close segments.

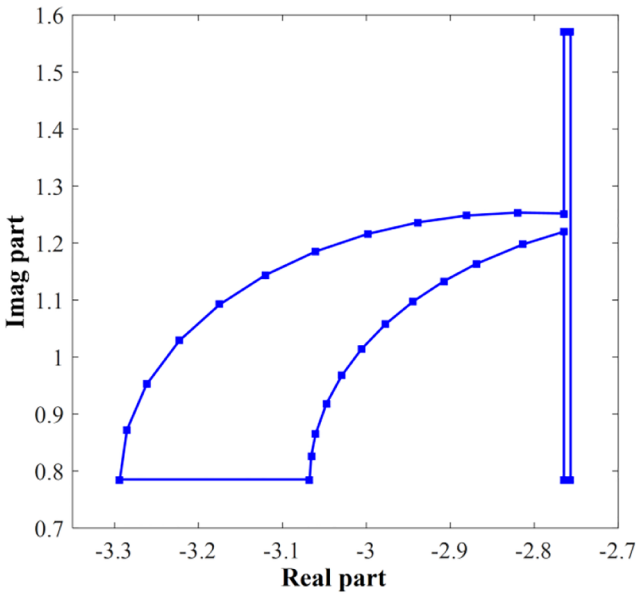

Fig. 15. Approximated geometry of a half FB in the Z-plane.

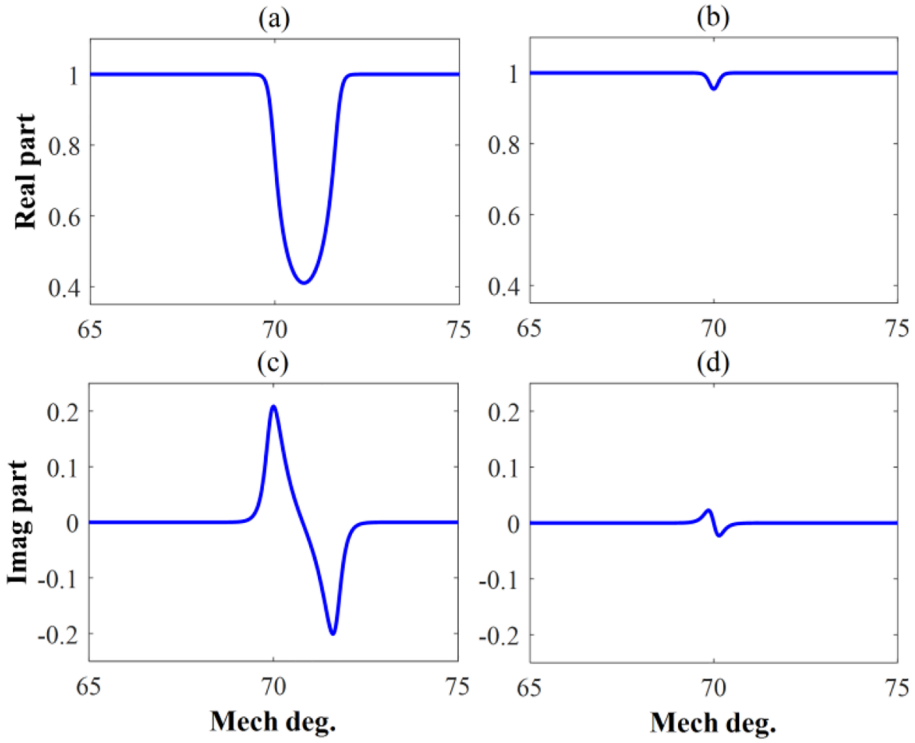

Fig. 16. (a),(b) Real (radial) and (c),(d) imaginary (tangential) components of complex air gap permeance for 2 (left) and 0.2 (right) degree end FB opening.

Fig. 16 shows the real and imaginary parts of the normalized permeances of the rotor FB for a tip that is open by 2 and 0.2 degrees. Similar to the effects of the stator slots, drop in the actual component of the permeance and change of direction in the imaginary component of the permeance are clearly seen at the ending position of the FB. It should be noted that the more open the FB end is, the greater will be its impact on the air gap field; and inversely, the narrower the FB, the lower its effect will become, to the extent that it may even be ignored.

3. Results and discussion

3.1. Torque calculation

Using the Maxwell Stress Tensor (MST) Method, the motor torque can be calculated as in (12) based on the magnetic field components [13].

$$T_{em} = \frac{2pl_a R_c^2}{\mu_0} \int_0^{\frac{\pi}{p}} B_r B_t d\theta \tag{12}$$

where p is the number of pole pairs, l_a is the effective length of the motor, and R_c is the radial distance of the air gap where closed path integral is placed on it. B_r and B_t represent the radial and tangential magnetic field components, respectively.

Fig. 17 summarizes the procedure used to calculate the SynRM field and shows the flowchart used to calculate the torque. Briefly, CMs are initially applied to the motor geometry to obtain the field generated by the stator windings based on the initial values of the currents. Using the stator radial field component and the MEC model, the rotor magnetic potential drop is then calculated for each FB. Depending on the angles of FB positions, the position of the virtual currents, whose values are equal to those of the rotor MMF, and their effects on the air gap field are determined. The air gap field will then be equal to the sum of the fields due to the stator and the FBs.

To simulate motor movement, rotor position must be changed with respect to the stator at each iteration. For this purpose, the air gap polygon is expanded by a pole pitch before and after the pole in which the field is being calculated. In this way, rotor virtual currents can be moved out of the pole region. The position of the rotor FB virtual currents changes for each rotor position thereby saving significant time as a result of relaxing the need for polygon change and repeat of the CM.

3.2. SynRM with three barrier per pole

In this Section, the proposed method is employed to calculate the torque of a SynRM containing a rotor with three FBs. Fig. 18 shows a rotor pole with three FBs and Fig. 19 shows the corresponding MEC model. In Fig. 18, the values α_1, α_2, and α_3 are 29, 19, and 6 degrees, respectively.

The parameters of the MEC model and the potential drop in each FB are calculated in the same way previously described in Section 2.2 for a rotor with a single FB. In the equivalent circuit of Fig. 19, the reluctances, R_g, are related to the air gap. R_{g1} includes a length from the air gap that contains the first FB. R_{g2L} and R_{g2R} are the air gap reluctances between two FBs with the magnetic reluctances R_{b1} and R_{b2} which have equal values due to their symmetry (step length equal to $\alpha_1 - \alpha_2$). Similarly, R_{g3L} and R_{g3R} are the left and right side air gap reluctances between the two FBs with the magnetic reluctances R_{b2} and R_{b3} which have equal values due to their symmetry (step lengths equal to $\alpha_2 - \alpha_3$).

The radial and tangential field components at time zero are shown

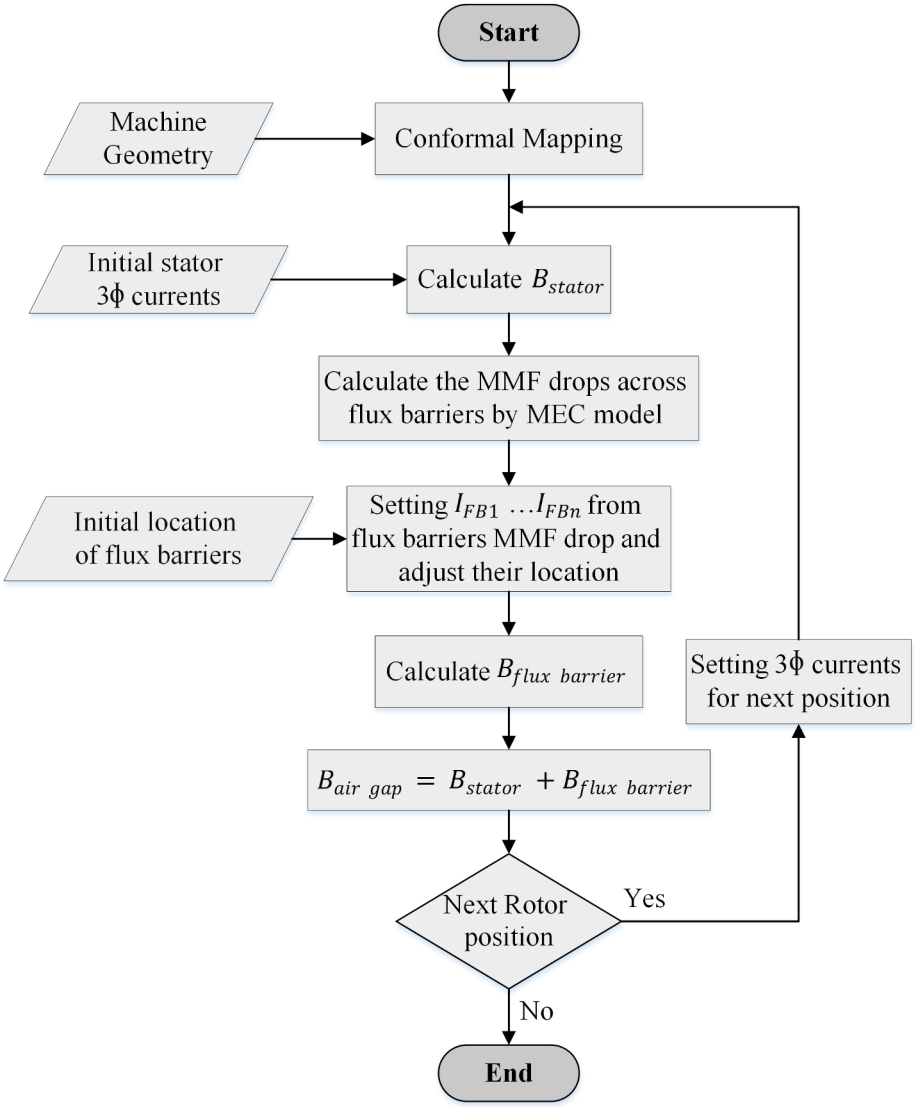

Fig. 17. Flow chart of proposed method for torque calculation.

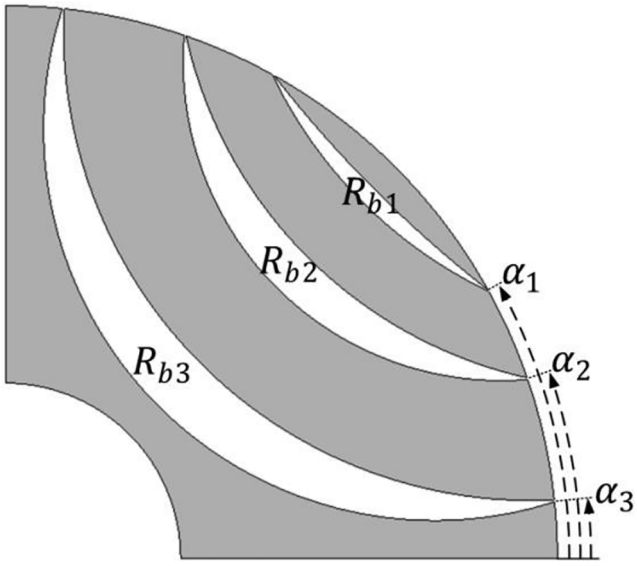

Fig. 18. SynRM rotor with three flux barriers.

in Figs. 20 and 21, respectively, based on the assumption that the rotor at time zero is in the direction of phase A axis and that three-phase currents are applied at a phase angle of 45 degrees to the stator windings. The three step drops in the fields are due to the three FBs. Changes in the tangential field due to FBs are indicated in Fig. 21. The radial and tangential field components closely follow the FEA results. The method proposed for calculating torque can be used to obtain the radial and tangential field components for each rotor position.

Fig. 22 presents the torque calculated through the MST using a closed path selected from the middle of the air gap. The continuous line in this Fig. represents the motor torque calculated by the proposed method for the three steps of the stator slot with a one-tenth mechanical degree step and the dashed line represents the torque calculated by FEA. Clearly, changes in the torque are exactly captured by the proposed method. The movement of virtual currents approximates rotor rotation accurately. The agreement between the results obtained from the two methods confirms the accuracy of the proposed method for calculating motor torque.

The average time to calculate the torque with the proposed method (with Intel Core i5 CPU 2.60 GHz processor, 8 GB RAM) is about 60 times faster than FEA using a fixed mesh with 33,000 triangular elements, which corresponds to the number of obtained elements for a

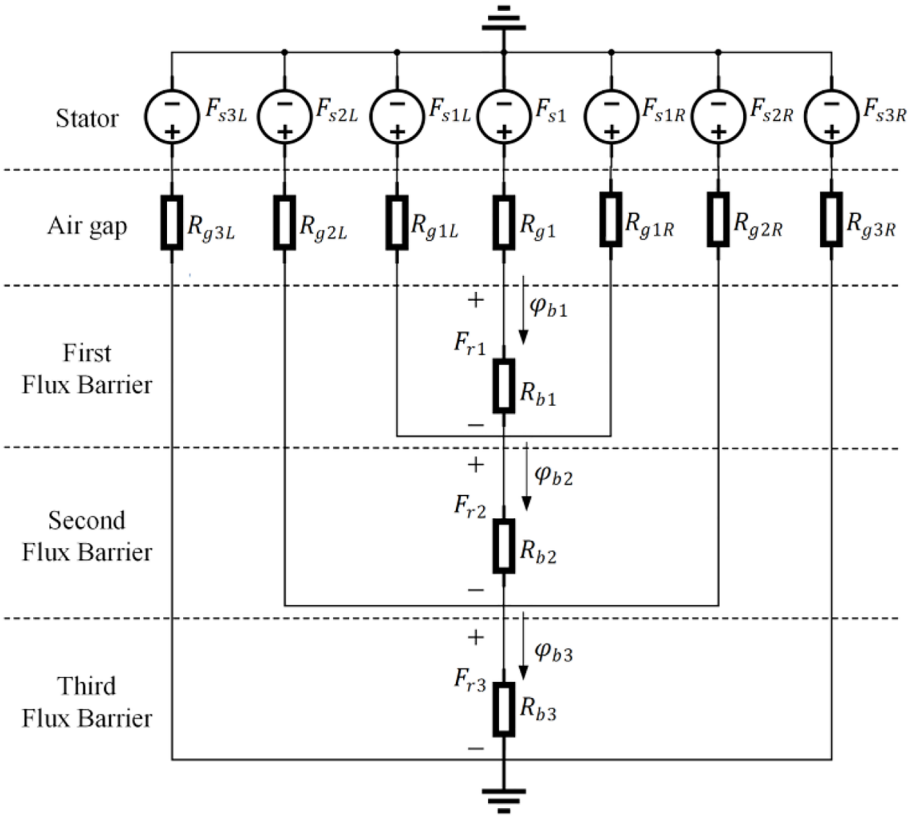

Fig. 19. MEC model of SynRM with three barriers per pole.

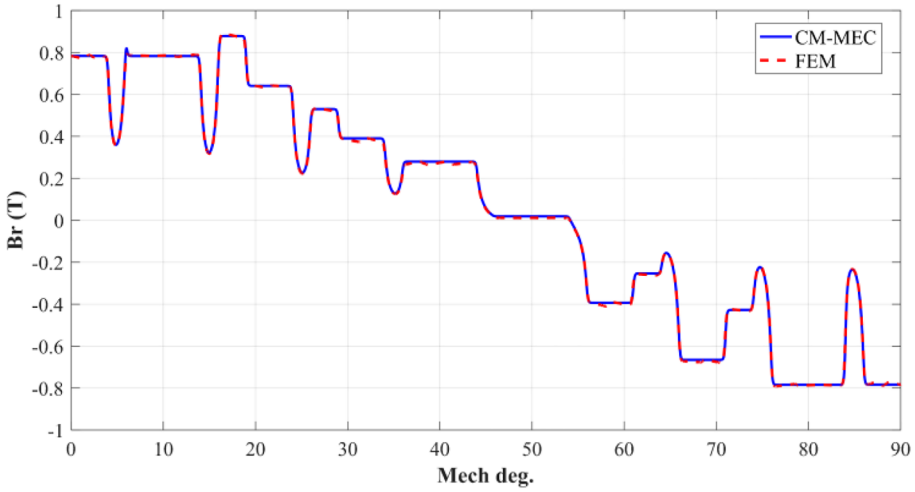

Fig. 20. Radial field component at zero instant.

0.01% error rate in the adaptive state. All codes for the proposed method has been implemented in MATLAB software and FEA calculations have been performed with ANSYS Maxwell software.

4. Conclusion

In this paper, SynRM field components in the air gap were analytically calculated using a combination of the CM and MEC method. The proposed combination takes into consideration both stator slotting and rotor FBs with rotor movement. In this method by introducing virtual currents for rotor potential drops, the tangential component of the field which is required for torque ripple calculation, is obtained. The accuracy of field and torque calculations by the proposed method was validated by comparing the results to those from FEA. It was shown that the proposed method not only enjoys high accuracy and high computation speed but also relaxes the need for building a geometrical model. The method can be, therefore, recommended as a useful technique for the rapid and accurate analysis of field components and for the initial design of SynRM.

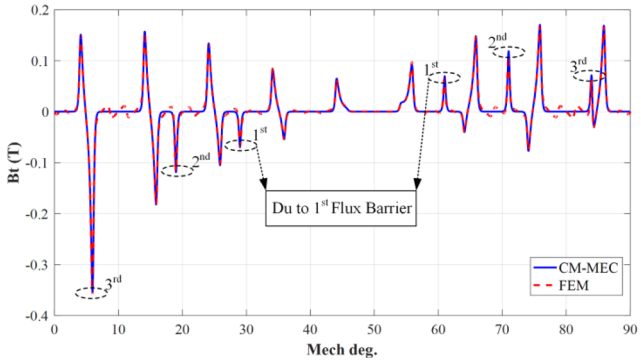

Fig. 21. Tangential field component at zero instant.

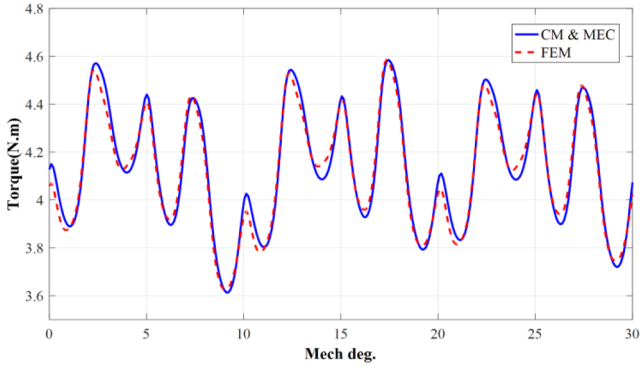

Fig. 22. Comparison of torque waveform obtained with proposed method and FEM.

Declaration of Competing Interest

The authors declare that they have no known competing financial interests or personal relationships that could have appeared to influence the work reported in this paper.

References

[1] A. Boglietti, A. Cavagnino, M. Pastorelli, A. Vagati, Experimental comparison of induction and synchronous reluctance motors performance, in: Fourtieth IAS Annual Meeting. Conference Record of the 2005 Industry Applications Conference, 2005, IEEE, 2005, pp. 474-479.

[2] G. Pellegrino, F. Cupertino, C. Gerada, Automatic design of synchronous reluctance motors focusing on barrier shape optimization, IEEE Trans. Ind. Appl. 51 (2014) 1465–1474.

[3] R.-R. Moghaddam, F. Gyllensten, Novel high-performance SynRM design method: An easy approach for a complicated rotor topology, IEEE Trans. Ind. Electron. 61 (2013) 5058–5065.

[4] C. López, T. Michalski, A. Espinosa, L. Romeral, Rotor of synchronous reluctance motor optimization by means reluctance network and genetic algorithm, in: 2016 XXII International Conference on Electrical Machines (ICEM), IEEE, 2016, pp. 2052–2058.

[5] C. López-Torres, A.G. Espinosa, J.-R. Riba, L. Romeral, Design and optimization for vehicle driving cycle of rare-earth-free SynRM based on coupled lumped thermal and magnetic networks, IEEE Trans. Veh. Technol. 67 (2017) 196–205.

[6] N. Bianchi, S. Bolognani, D. Bon, M. Dai Pre, Rotor flux-barrier design for torque ripple reduction in synchronous reluctance motors, in: Conference Record of the 2006 IEEE Industry Applications Conference Forty-First IAS Annual Meeting, IEEE, 2006, pp. 1193-1200.

[7] C. López Torres, G. Bacco, N. Bianchi, A. Espinosa, J.L. Romeral Martínez, A parallel analytical computation of synchronous reluctance machine, (2018).

[8] A. Tessarolo, Modeling and analysis of synchronous reluctance machines with circular flux barriers through conformal mapping, IEEE Trans. Magn. 51 (2014) 1–11.

[9] H. Mahmoud, G. Bacco, M. Degano, N. Bianchi, C. Gerada, Synchronous reluctance motor iron losses: considering machine nonlinearity at MTPA, FW, and MTPV operating conditions, IEEE Trans. Energy Convers., 33 (2018) 1402–1410.

[10] G. Bacco, N. Bianchi, H. Mahmoud, A nonlinear analytical model for the rapid prediction of the torque of synchronous reluctance machines, IEEE Trans. Energy Convers. 33 (2018) 1539–1546.

[11] T.C. O'Connell, P.T. Krein, A Schwarz–Christoffel-based analytical method for electric machine field analysis, IEEE Trans. Energy Convers. 24 (2009) 565–577.

[12] H. Mirahki, M. Moallem, M. Ebrahimi, B. Fahimi, Combined ON/OFF and conformal mapping method for magnet shape optimisation of SPMSM, IET Electr. Power Appl. 12 (2018) 1365–1370.

[13] K. Boughrara, D. Zarko, R. Ibtiouen, O. Touhami, A. Rezzoug, Magnetic field analysis of inset and surface-mounted permanent-magnet synchronous motors using Schwarz-Christoffel transformation, IEEE Trans. Magn. 45 (2009) 3166–3178.

[14] L. Gu, E. Bostanci, M. Moallem, S. Wang, P. Devendra, Analytical calculation of the electromagnetic field in SRM using conformal mapping method, in: 2016 IEEE Transportation Electrification Conference and Expo (ITEC), IEEE, 2016, pp. 1-6.

[15] H. Mirahki, M. Moallem, Analytical prediction of cogging torque for interior permanent magnet synchronous machines, Prog. Electromagnetics Res. 37 (2014) 31–40.

[16] D.-K. Lim, K.-P. Yi, D.-K. Woo, H.-K. Yeo, J.-S. Ro, C.-G. Lee, H.-K. Jung, Analysis and design of a multi-layered and multi-segmented interior permanent magnet motor by using an analytic method, IEEE Trans. Magn. 50 (2014) 1–8.

[17] A. Hanic, D. Zarko, D. Kuhinek, Z. Hanic, On-load analysis of saturated surface permanent magnet machines using conformal mapping and magnetic equivalent circuits, IEEE Trans. Energy Convers. 33 (2018) 915–924.

[18] A. Hanic, D. Zarko, Z. Hanic, A novel method for no-load magnetic field analysis of saturated surface permanent-magnet machines using conformal mapping and magnetic equivalent circuits, IEEE Trans. Energy Convers. 31 (2015) 740–749.

[19] A. Tessarolo, M. Degano, N. Bianchi, On the analytical estimation of the airgap field in synchronous reluctance machine, in: 2014 International Conference on Electrical Machines (ICEM), IEEE, 2014, pp. 239–244.

[20] M. Pohl, D. Gerling, Analytical Model of Synchronous Reluctance Machines with Zhukovski Barriers, in: 2018 XIII International Conference on Electrical Machines (ICEM), 2018, pp. 91-96.

[21] H. Mahmoud, N. Bianchi, Nonlinear analytical model of eccentric synchronous reluctance machines considering the iron saturation and slotting effect, IEEE Trans. Ind. Appl. 53 (2017) 2007–2015.

[22] H. Shao, S. Li, T.G. Habetler, Analytical Calculation of the Air-gap Flux Density and Magnetizing Inductance of Synchronous Reluctance Machines, in: 2018 IEEE Energy Conversion Congress and Exposition (ECCE), 2018, pp. 5408-5413.

[23] T.A. Driscoll, L.N. Trefethen, Schwarz-christoffel Mapping, Cambridge University Press, 2002.

[24] T. Driscoll, Schwarz-Christoffel Toolbox User's Guide: Version 2.3, Department of Mathematical Sciences, Ewing Hall, University of Delaware, Newark, DE, 19716 (2005).